Journal of Power Sources 196 (2011) 4555–4563

Contents lists available at ScienceDirect

Journal of Power Sources

journal homepage: www.elsevier.com/locate/jpowsour

Quantitative evaluation of solid oxide fuel cell porous anode microstructure based on focused ion beam and scanning electron microscope technique and prediction of anode overpotentials

Masashi Kishimoto*, Hiroshi Iwai, Motohiro Saito, Hideo Yoshida

Department of Aeronautics and Astronautics, Kyoto University, Yoshida Honmachi, Sakyo-ku, Kyoto 606-8501, Japan

ARTICLE INFO

Article history:
Received 29 August 2010
Received in revised form
19 December 2010
Accepted 28 December 2010
Available online 12 January 2011

Keywords:
SOFC
Microstructure
FIB–SEM
Random walk
Numerical simulation

ABSTRACT

A three-dimensional microstructure of a solid oxide fuel cell (SOFC) anode is directly observed by a focused ion beam and scanning electron microscope (FIB–SEM) technique. Microstructural parameters, which are closely related to transport phenomena and electrochemical reaction in a porous anode, are quantitatively evaluated, such as volume fraction, percolation probability, tortuosity factor, surface-to-volume ratio, and three-phase boundary density. A random-walk-based diffusion simulation is effectively used for quantification. As an application of the quantified parameters, 1D numerical simulation of a SOFC anode is conducted. The predicted anode overpotential agrees well with the experimental counterparts in the condition of 3.0% H_2O–97% H_2, 1273 K, while it is overestimated at high humidified and low temperature conditions.

1. Introduction

The increasing demand for high efficiency and low pollution energy conversion systems has created significant interest in fuel cells. Solid oxide fuel cells (SOFCs) are receiving attentions not just because of their high efficiency but also because of their fuel flexibility. SOFC electrodes commonly consist of porous materials, and their microstructure has a significant influence on the power generation performance and durability of the electrodes. Ni–YSZ cermet is the most widely used for an anode, which consists of electron-conductive Ni phase and oxide-ion-conductive YSZ phase. During electric generation, many phenomena occur simultaneously in the porous anode—gas diffusion in the pore phase, electron transport in the Ni phase, and oxide-ion transport in the YSZ phase. Also, electrochemical reaction in the SOFC anode occurs at the "three-phase boundary" (TPB). Therefore, the anode microstructure should be fabricated so that it includes as much TPB as possible. In addition, the connectivity and structural complexity of each phase should be considered for sufficient transport through each phase.

Owing to the importance of microstructure, many researches have been devoted to the investigation of the porous structure, and to evaluate the performance of electrodes based on the porous microstructure. It is a common practice today to use cross-sectional 2D images [1,2]. From these images, 3D microstructural parameters are estimated by using porous models based on geometric theories, such as the general effective media (GEM) theory [3], the concept of contiguity (CC) [4,5], the random register network model [6] and the random packing spheres model [7]. However, these models include some assumptions, such as random mixture of sphere particles, so their applicabilities should be carefully considered.

Recently, the focused ion beam and scanning electron microscope (FIB–SEM) technique is gathering attention as a break through of the direct 3D observation of porous structure [8–11]. It enables observation of many sequential 2D images of a porous structure and reconstruction of the 3D structure in a computational field. The X-ray tomography [12] is also available for the 3D observation. Its spatial resolution is gradually improved and applicable for the sub-micron investigation. From the reconstructed structure, we can directly evaluate the microstructural parameters without assumptions needed in the above methods based on 2D images. These parameters directly obtained from the real electrode 3D structure are the key to consider the relationships between porous microstructures and the cell power generation performance.

Matsui et al. [13] experimentally investigated the cell degradation phenomena observed under high steam concentration condition. They observed the 3D microstructure obtained by FIB–SEM technique before and after the experiment and discussed the correlation between the microstructure change and degradation. Another promising application of 3D structure is numerical simulations. Development of a reliable simulation model to predict

* Corresponding author. Tel.: +81 75 753 5203; fax: +81 75 753 52.
E-mail address: blauer-vogel@t04.mbox.media.kyoto-u.ac.jp (M. Kishimoto).

0378-7753/$ – see front matter © 2011 Elsevier B.V. All rights reserved.
doi:10.1016/j.jpowsour.2010.12.100

Nomenclature

D	diffusion coefficient ($m^2\ s^{-1}$)
d_h	hydraulic diameter (m)
d_p	mean pore diameter (m)
E	electric potential (V)
F	Faraday constant ($C\ mol^{-1}$)
i_0	exchange current density per unit volume ($A\ m^{-3}$)
$i_{0,tpb}$	exchange current per unit TPB length ($A\ m^{-1}$)
K	permeability (m^2)
L	Anode thickness (m)
l_{tpb}	TPB density ($m\ m^{-3}$)
M	molar weight ($kg\ mol^{-1}$)
N	molar flux ($mol\ m^{-2}\ s^{-1}$)
n	number of electron
P	partial pressure (Pa)
Q	probability
R	gas constant ($J\ mol^{-1}\ K^{-1}$)
S	surface area (m^2)
T	temperature (K)
V	volume fraction
X	molar ratio

Greek symbols

Γ	transport rate
β	transfer coefficient
η	overpotential (V)
μ	viscosity (Pa s)
σ	conductivity ($m^2\ s^{-1}$)
$\Sigma\nu$	diffusion volume (m^3)
τ	tortuosity factor
Φ, ϕ	electric potential (V)

Subscripts

act	activation
ave	average
bulk	bulk fluid
con	concentration
el	electron
eq	equilibrium
H_2	hydrogen
H_2O	steam
io	ion
K	Knudsen
O_2	oxygen
t	total
tpb	three-phase boundary
0	standard state

Superscripts

eff	effective value in porous media
eq	equilibrium
iso	isolated phase

the electrode/cell performance is also required for investigating the microstructural effect on the power generation performance. In the early stage when quantitative data of the microstructure were not available, micro models, such as random packing model [7], were often used. However, a direct application of the measured microstructural information is enabled by FIB–SEM observation. Shikazono et al. [14] recently applied the Lattice Boltzmann Method to predict the anode polarization characteristics by using 3D microstructure from FIB–SEM. A full 3D simulation, however, requires a large computational resource. Wilson et al. [15] carried out 1D simulation based on Tanner–Fung–Virkar model to predict the polarization resistance of LSM–YSZ cathode. The geometric parameters were evaluated from FIB–SEM data.

In this paper, we directly observe the three-dimensional microstructure of the porous Ni–YSZ cermet anode by FIB–SEM. From the obtained images, we evaluate the microstructural parameters which characterize the porous structure, such as volume fraction, percolation probability, tortuosity factor, surface-to-volume ratio, and three-phase boundary density. In particular, random-walk-based diffusion simulation is applied in quantification of tortuosity factors [16,17]. A 1D numerical simulation to predict the anode polarization characteristics is conducted without using any micro model but directly applying the microstructural parameters evaluated from the reconstructed 3D structure, which is expected to improve the reliability of numerical simulations. Predicted anode overpotentials are compared with the experimental results of the single cell test.

2. Experimental

2.1. Sample preparation

In this study, we examine the Ni–YSZ cermet anode (Ni:YSZ = 50:50 vol.%, YSZ:8 mol% Y_2O_3–ZrO_2) of conventional button cell, Ni–YSZ|YSZ|LSM. The anode material, NiO–YSZ, is mixed with polyethylene glycol, screen-printed on a YSZ disk electrolyte (Thickness: 500 μm, TOSOH Co.), and sintered at 1673 K for 5 h. The $(La_{0.8}Sr_{0.2})_{0.97}MnO_3$ (abbreviated as LSM) cathode is also mixed with polyethylene glycol to form slurry. It is then screen-printed on the other face of the electrolyte and sintered at 1423 K for 5 h. After the anode of the test cell is reduced at 1273 K, the cell temperature is lowered to room temperature and the anode is supplied to the FIB–SEM observation as a sample. The sample is infiltrated with epoxy resin (Marumoto Struers KK) under vacuum conditions so that the pores of the porous electrode can be easily distinguished during SEM observation. Cured sample is polished using an Ar-ion beam cross-section polisher (JEOL Ltd., SM-09010) and provided to the FIB–SEM (Carl Zeiss, NVision 40) observation.

2.2. FIB–SEM imaging

The 3D microstructure of the Ni–YSZ anode is observed by the FIB–SEM system. The FIB–SEM system, NVision 40, is equipped with a Gemini FE-SEM column (Zeiss), a zeta FIB column (SIINT) and a multichannel gas injection system (SIINT). An in-lens secondary electron detector is used for the microstructural observation with an acceleration voltage around 1–2 kV. Fig. 1 shows an example of the obtained cross-sectional image. The observation is conducted at three different locations of a sample anode.

2.3. 3D reconstruction

The set of cross-sectional images obtained by the FIB–SEM tends to include misalignment between the images, which is unfavorable for 3D reconstruction and quantification conducted afterwards. Therefore, we put some lines on the sample surface and use them for an alignment mark.

Because of the different hardnesses of the porous components, uniform milling of the observation surface is difficult. Some vertical lines, which are caused by undesired milling with the FIB, often appear on the lower half of the cross-section. They sometimes cause local brightness change or distort the microstructure. Therefore, we extract regions available for the later analysis. The sample sizes and voxel sizes of the extracted region are summarized in Table 1.

The phase separation is conducted based on the brightness of the images. Preliminary to the phase separation, we use an energy

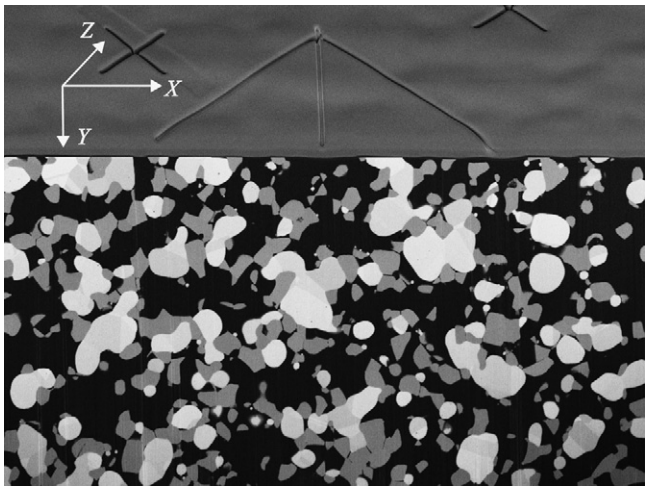

Fig. 1. Example of the cross-sectional image obtained by FIB–SEM.

Table 1
Sample sizes and voxel sizes of extracted region.

	X	Y	Z
Sample 1			
Sample size [μm]	25.4	10.4	4.56
Voxel size [nm]	26.6	26.6	60.0
Sample 2			
Sample size [μm]	19.2	8.51	6.20
Voxel size [nm]	26.6	26.6	62.0
Sample 3			
Sample size [μm]	26.7	10.3	6.05
Voxel size [nm]	26.5	26.5	72.0

dispersive X-ray fluorescence spectrometer (EDX) to identify the components of the porous anode. In the images, white, gray and black parts corresponded to Ni, YSZ and pore phases, respectively (see Fig. 1).

After the alignment and the phase separation, the sequential set of the 2D images is lined up with the actual increment and the 3D microstructure is reconstructed in a virtual field. Fig. 2 shows the reconstructed microstructure of the porous anode. We use the commercial image processing software, Avizo (Mercury Computer Systems, Inc.), for the phase separation, 3D reconstruction, and some of the quantification explained afterward.

2.4. Electrochemical characterization

The power generation performance test of a cell that is made in the same way as the observed sample is conducted. A platinum reference electrode is attached so as to surround the side edge of the thin electrolyte disk. The single cell is sandwiched by alumina tubes with Pyrex glass seal as shown in Fig. 3. Before the electrochemical measurements, NiO–YSZ was reduced under hydrogen atmosphere at 1273 K. Then, the power generation is conducted for 3 h at the terminal voltage 0.7 V to stabilize the initial performance. Feeding gas is 3% H_2O–97% H_2 and Air (79% N_2–21% O_2) to anode and cathode, respectively.

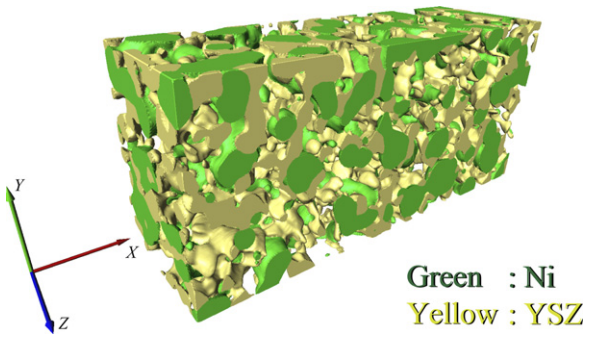

Fig. 2. Three-dimensional microstructure of a porous anode.

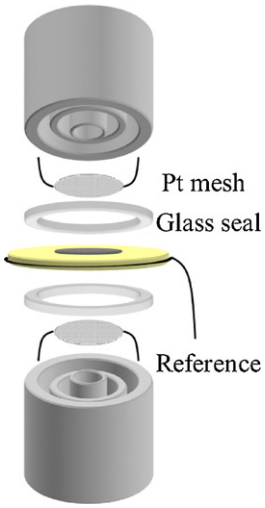

Fig. 3. Schematic drawing of a single cell test.

A gaseous mixture of H_2–H_2O is supplied to anode with a total flow rate of 100 ml min^{-1}. The mixture gas is prepared by bubbling H_2 through water which was kept at various temperatures. Air is supplied to cathode with a flow rate of 100 ml min^{-1}. Current-voltage characteristics and AC impedance measurements are conducted at 1073, 1173 and 1273 K using the Solatron 1287 electrochemical interface and Solatron 1255 frequency analyzer. The applied frequency is in the range of 0.1 Hz to 1 MHz with the voltage amplitude of 10 mV.

3. Quantification of microstructure of porous electrode

From the phase-separated images, the 3D microstructure of the porous anode is virtually reconstructed in a computational field and microstructural parameters are quantified. They are expected to be the keys to correlating the microstructure with the power generation performance of the anode.

3.1. Volume fraction

Volume fraction is the most primary information of porous materials and has strong relationships with other microstructural parameters. We simply count the voxels corresponding to each phase, and calculate the percentage of the voxels.

3.2. Percolation probability

Although it seems natural that higher volume fraction is preferable for sufficient transport through the porous media, connectivity of each phase should also be considered. Wilson et al. [18] employed a simple and clear definition of connectivity and discussed by classifying a phase of interest into three categories: connected, isolated and unknown. In this study, we define the percolation probability of phase i, Q_i, as the volume percentage of the region which penetrates the cuboid sample volume in a certain direction, x-, y- or z-direction, so that we can consider the anisotropic aspect of a porous structure. Therefore, we define the percolation probability

as follows:

$$Q_i^{\text{eff}} = \frac{V_i^{\text{eff}}}{V_i} \tag{1}$$

where V_i denotes the volume fraction of the phase i and superscript eff indicates the penetrating region. And we also consider the isolated region, which does not touch any boundary of the cuboid sample volume, and calculate the percentage of the region:

$$Q_i^{\text{iso}} = \frac{V_i^{\text{iso}}}{V_i} \tag{2}$$

where the superscript iso indicate the isolated region.

3.3. Tortuosity factor

In porous materials, transport rates are generally reduced compared with that in free space. It is primarily caused by the decrease of the conductive volume but that is not the only reason. We should pay attention to the structural complexity of the phase. The effective transport rate can generally be written as follows:

$$\Gamma_i^{\text{eff}} = \frac{V_i}{\tau_i}\Gamma_i \tag{3}$$

where the V_i and τ_i are the volume fraction and the tortuosity factor of phase i, respectively. And Γ_{i} is the bulk transport rate. We have to keep it in mind that "tortuosity factor" and "tortuosity" are different. For a simple explanation, we exemplify the case of curved channel as depicted in Fig. 4. The "tortuosity" is defined as the ratio of the length of the curved channel, L', to that of the straight channel, L. On the other hand, the "tortuosity factor" in this simple example is the square of the tortuosity. Both represent the complexity of porous materials. In a real porous structure, however, there are many branches and communications of the transport paths, which makes it impossible to define clearly a transport path length. What is important in practice is to find a reliable "tortuosity factor" expressed in a form of Eq. (3).

The tortuosity factor can be quantitatively evaluated by a diffusion simulation based on the random walk calculation [16,17]. In the first step of the method, a large number of imaginary particles are randomly distributed in the considered phase, i.e., the Ni, YSZ, or pore phase. Each walker randomly chooses one of the neighboring voxels as its possible location in the next time step. If the selected neighboring voxel is the same as the considered phase, the walker migrates to that voxel. If the selected voxel is a different phase, the walker stays at the current voxel and waits for the next time step. In this procedure, neither absorption nor desorption on the phase boundaries is considered. While repeating this process, the mean square displacement of the random walkers is calculated as follows:

$$\langle r^2(t)\rangle = \frac{1}{n}\sum_{i=1}^{n}[\{x_i(t)-x_i(0)\}^2+\{y_i(t)-y_i(0)\}^2+\{z_i(t)-z_i(0)\}^2] \tag{4}$$

where n is the total number of random walkers, and $x_i(t)$, $y_i(t)$, and $z_i(t)$ are the 3D coordinates of the walker's position at time t for the ith walker. The X–Y plane is embedded on a 2D SEM image and Z is the proceeding direction of the FIB–SEM observation process. $\langle\,\rangle$ indicates an ensemble average over all the walkers. Since the mean square displacement $\langle r^2\rangle$ is proportional to time, the transport rate of the imaginary particles is related to the time derivative of $\langle r^2\rangle$ and the volume fraction of phase i:

$$\Gamma_i = V_i\frac{1}{6}\frac{d\langle r^2(t)\rangle_i}{dt} \tag{5}$$

The mean square displacement in porous media is lower than that obtained in a free space because the movement of the particles is interrupted at the phase boundaries. The degree of the reduction is measured quantitatively using the tortuosity factor defined as

$$\tau_i = \frac{\Gamma_{\text{bulk}}}{\Gamma_i^{\text{eff}}/V_i} = \frac{V_i}{V_i^{\text{eff}}}\frac{d\langle r^2(t)\rangle_{\text{bulk}}}{dt}\Big/\frac{d\langle r^2(t)\rangle_i}{dt} \tag{6}$$

where Γ_i^{eff} and V_i^{eff} are the transport rate and volume fraction of the penetrating region, respectively. It should be noted that the random walkers are distributed only in the penetrating region of each phase because the isolated region cannot contribute to the transport phenomena. Otherwise, tortuosity factors are overestimated.

When porous media have an anisotropic structure, the mean square displacement $\langle r^2\rangle$ may be divided into the directional mean square displacements $\langle x^2\rangle$, $\langle y^2\rangle$, and $\langle z^2\rangle$. The anisotropic tortuosity factors are calculated with similar relations, such as Eqs. (5) and (6).

3.4. Surface-to-volume ratio

Surface-to-volume ratio is also an important factor, particularly in heat transfer and/or chemical reactions. The larger the parameter, the larger the surface area that is included in the porous media: such a large surface area may result in more heat exchange and surface reaction. At the same time, a larger surface-to-volume ratio causes complexity of the porous structure, limiting the transport through the phase.

The surface area obtained by using the Avizo image processing software includes the surface on the boundary of the observed region, which is not an actual surface area. Therefore we substitute the boundary surface and calculate the surface area truly included in the observed region, and then obtain the surface-to-volume ratio. It should be noted that the surface-to-volume ratio is different from the "specific surface." In the former case, the denominator of the ratio is the volume of the considered phase instead of the whole volume of the cuboid region.

3.5. Three-phase boundary (TPB) density

We adopt the "volume expansion method" to evaluate the TPB density [11]. We slightly expand each phase in the computational domain and extract the overlapping region as the "TPB existing region". This region has a string-like form and contains the TPB lines inside it. The centerlines of those strings are considered as TPBs and their lengths are measured.

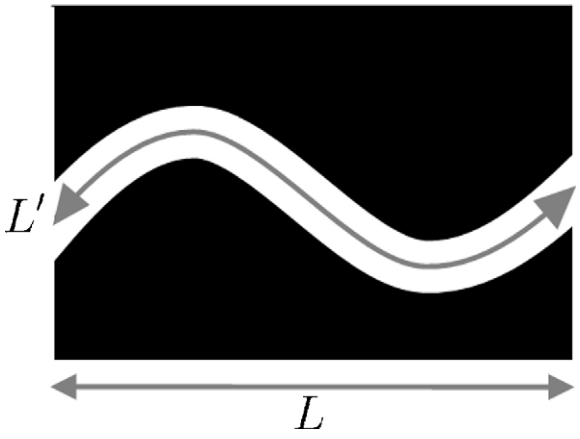

Fig. 4. Simple curved channel for the explanation of tortuosity and tortuosity factor.

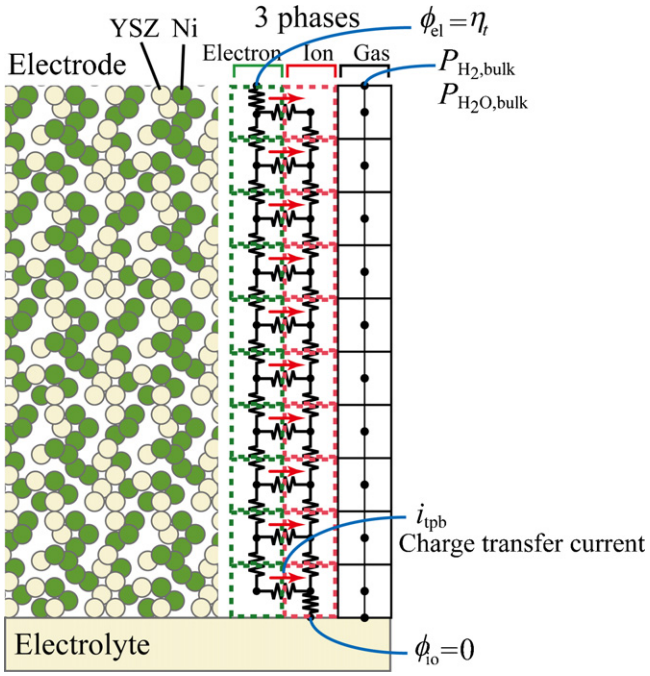

Fig. 5. Schematic picture of calculation model.

4. Numerical simulation

We conduct a numerical simulation with microstructural parameters obtained from the 3D microstructure of the anode, and compare the power generation performance with the experimental counterparts. The simulation is based on finite volume method (FVM), and is conducted in the thickness direction of the anode. We consider the conservation of electric potential and gas components and also electrochemical oxidation of hydrogen. Temperature is assumed to be uniform in the anode. Schematic picture of the calculation model is shown in Fig. 5.

4.1. Ion and electron transport

In the SOFC anodes, electrons and oxide ions are transported through the Ni phase and YSZ phase, respectively. Considering the conservation of these species, the following equations are introduced as governing equations:

$$\nabla\cdot(\sigma_{el}^{eff}\nabla\phi_{el}) = -i_{tpb} \tag{7}$$

$$\nabla\cdot(\sigma_{io}^{eff}\nabla\phi_{io}) = i_{tpb} \tag{8}$$

where ϕ_{el} and ϕ_{io} are the electric potential in electron conductive phase (Ni) and oxide ion conductive phase (YSZ), respectively, and i_{tpb} is the current exchanged between the two phases. σ_{el}^{eff} and σ_{io}^{eff} are effective electron/ion conductivities, which we define as follows:

$$\sigma_{el}^{eff} = \frac{V_{el}}{\tau_{el}}\sigma_{el}, \quad \sigma_{io}^{eff}\sigma = \frac{V_{io}}{\tau_{io}}\sigma_{io} \tag{9}$$

where V_i and τ_i are the volume fraction and tortuosity factor of the phase i. And σ_{el} and σ_{io} are the conductivities of the bulk materials obtained from literatures [19,20].

4.2. Diffusion of gas species

The dusty-gas model (DGM) [21,22] is available to simulate multi-component gas diffusion in porous materials, such as SOFC electrodes. This model includes the flow induced by a total pressure gradient and can also be used in the situation where the effect of Knudsen diffusion is not negligible. The DGM is written as an implicit relationship among the molar fraction, molar flux, and total pressure gradient:

$$\frac{N_i}{D_{i,K}^{eff}} + \sum_{j=1,j\neq i}^{n}\frac{X_jN_i - X_iN_j}{D_{ij}^{eff}} = -\frac{P_i}{RT}\nabla X_i - \frac{X_i}{RT}\left(1+\frac{KP_t}{\mu D_{i,K}^{eff}}\right)\nabla P_i \tag{10}$$

where X_i, P_i and N_i are the molar fraction, partial pressure and molar flux of gas species i. P_t is the total pressure. μ and K are the mixture viscosity and permeability, and $D_{i,K}^{eff}$ and D_{ij}^{eff} are the effective Knudsen diffusion coefficients and the effective binary diffusion coefficients, respectively.

The Eq. (10) can be reduced to the explicit form of the molar fluxes by solving linear simultaneous equations.

$$N_i = -\sum_{j=1}^{n}\frac{l_{ij}}{RT}\left(\nabla P_j + \frac{KP_j}{\mu D_{j,K}^{eff}}\nabla P_t\right) \tag{11}$$

where l_{ij} are defined as the matrix of diffusion coefficients and can be represented as a matrix inverse:

$$l_{ij} = h_{ij}^{-1} \tag{12}$$

where the elements of matrix H are defined as follows:

$$h_{ij} = \left[\frac{1}{D_{i,K}^{eff}} + \sum_{k=1,k\neq i}^{n}\frac{X_k}{D_{ik}^{eff}}\right]\delta_{ij} + (\delta_{ij}-1)\frac{X_i}{D_{ij}^{eff}} \tag{13}$$

The effective Knudsen diffusion coefficients $D_{i,K}^{eff}$ and the effective binary diffusion coefficients D_{ij}^{eff} in the porous anode are estimated by using the volume fraction and tortuosity factor of the pore phase:

$$D_{i,K}^{eff} = \frac{V_{pore}}{\tau_{pore}}D_{i,K}, \quad D_{ij}^{eff} = \frac{V_{pore}}{\tau_{pore}}D_{ij} \tag{14}$$

The bulk Knudsen diffusion coefficients are estimated as

$$D_{i,K} = \frac{d_p}{2}\frac{2}{3}\sqrt{\frac{8RT}{\pi M_i}} \tag{15}$$

where d_p is the mean pore diameter, which is assumed to be the same as the hydraulic diameter d_h, and is described using the surface-to-volume ratio of the pore phase:

$$d_p \approx d_h = \frac{4}{(S/V)_{pore}} \tag{16}$$

For the binary diffusion coefficients, the Fuller–Schettler–Giddings' equation [23] is adopted in this study:

$$D_{ij} = \frac{0.01013T^{1.75}\left((1/M_i\times10^3)+(1/M_j\times10^3)\right)^{1/2}}{P\left[\left(\Sigma v_i\times10^6\right)^{1/3}+\left(\Sigma v_j\times10^6\right)^{1/3}\right]^2} \tag{17}$$

where M_i is the molecular mass, and Σv_i represents the diffusion volume of the molecules of species i [24].

Permeability of the porous anode is also necessary to consider the Darcy flow. Among many ways to estimate the parameter [25], we adopt the following relationship to directly use the microstructural parameters evaluated in this study [17]:

$$K = \frac{V_{pore}}{6\tau_{pore}(S/V)_{pore}^2} \tag{18}$$

In this formula, the porous network is considered as a group of curved tubes, whose diameters are uniform and given by Eq. (16),

and the flow inside is assumed to be a Poiseuille flow. By comparing the Darcy's law with the Poiseuille's law, the above formula is obtained.

4.3. Electrochemical reaction

In SOFC anodes, electrochemical oxidation of hydrogen takes place at the TPBs, and steam and electrons are generated. Local charge-transfer rate for the hydrogen oxidation within the anode can be represented by Butler–Volmer equation as

$$i_{\mathrm{tpb}} = i_0 \left[\exp\left(\frac{\beta n F}{RT} \eta_{\mathrm{act}} \right) - \exp\left(-\frac{(1-\beta) n F}{RT} \eta_{\mathrm{act}} \right) \right] \tag{19}$$

where i_0 is the exchange current density, that is the current density generated in the anodic and cathodic reaction at the equilibrium condition. β is the transfer coefficient, which varies from 0 to 1 depending on the transition state in the electrochemical reaction. In this study, we set the value as 0.5. n is the number of electrons participating in the electrochemical reaction, which is 2 in this study. F is the Faraday constant and η_{act} is the activation overpotential defined as follows:

$$\eta_{\mathrm{act}} = E - E^{\mathrm{eq}} = \Phi_{\mathrm{el}} - \Phi_{\mathrm{io}} - E_0^{\mathrm{eq}} - \frac{RT}{2F} \ln\left(\frac{P_{\mathrm{H_2O,bulk}}}{P_{\mathrm{H_2,bulk}}} \right) - \frac{RT}{2F} \ln\left(\frac{P_{\mathrm{H_2,bulk}}}{P_{\mathrm{H_2}}} \frac{P_{\mathrm{H_2O}}}{P_{\mathrm{H_2O,bulk}}} \right) \tag{20}$$

where $E = \Phi_{\mathrm{el}} - \Phi_{\mathrm{io}}$ is the electric potential difference between the electronic and ionic phases in the operating condition. E^{eq} is the electric potential difference between the two phases at the equilibrium, and E_0^{eq} is that in the standard state. In this study, we introduce following variables to rewrite Eq. (20) [26]:

$$\phi_{\mathrm{el}} = \Phi_{\mathrm{el}} \tag{21}$$

$$\phi_{\mathrm{io}} = \Phi_{\mathrm{io}} + E_0^{\mathrm{eq}} + \frac{RT}{2F} \ln\left(\frac{P_{\mathrm{H_2O,bulk}}}{P_{\mathrm{H_2,bulk}}} \right) \tag{22}$$

$$\eta_{\mathrm{act}} = \phi_{\mathrm{el}} - \phi_{\mathrm{io}} - \eta_{\mathrm{con}} \tag{23}$$

$$\eta_{\mathrm{con}} = \frac{RT}{2F} \ln\left(\frac{P_{\mathrm{H_2,bulk}}}{P_{\mathrm{H_2}}} \frac{P_{\mathrm{H_2O}}}{P_{\mathrm{H_2O,bulk}}} \right) \tag{24}$$

By using these variables, we can simply express the electric potential difference as the sum of the activation overpotential η_{act} and the concentration overpotential η_{con}.

The exchange current density i_0 in the Buttler–Volmer Eq. (19) strongly depends on the microstructure of the anode, and is considered to have a linear dependency on the TPB density l_{tpb}:

$$i_0 = i_{0,\mathrm{tpb}} l_{\mathrm{tpb}} \tag{25}$$

where $i_{0,\mathrm{tpb}}$ is the exchange current per unit TPB length. We use an empirical relationship for the $i_{0,\mathrm{tpb}}$ [27,28]:

$$i_{0,\mathrm{tpb}} = 31.4 P_{\mathrm{H_2}}^{-0.03} P_{\mathrm{H_2O}}^{0.4} \exp\left(-\frac{18300}{T} \right) \tag{26}$$

4.4. Boundary conditions

Boundary conditions used in the calculation are summarized in Table 2. Gas compositions are constant on the anode surface to represent the supplied fuel composition. In order to determine the anode overpotential, the electric potential in the Ni phase at the anode surface and that in the YSZ phase at the anode–electrolyte interface are properly set. Also, no flux conditions are set on the anode surface for the ionic potential and on the anode–electrolyte interface for gas components and electric potential.

Table 2
Boundary conditions.

Parameter	Surface ($x=0$)	Interface ($x=L$)
Total pressure	$P_t(0) = P_{t,\mathrm{bulk}}$	$\frac{dP_t}{dx}(L) = 0$
H_2 partial pressure	$P_{\mathrm{H_2}}(0) = P_{\mathrm{H_2,bulk}}$	$\frac{dP_{\mathrm{H_2}}}{dx}(L) = 0$
H_2O partial pressure	$P_{\mathrm{H_2O}}(0) = P_{\mathrm{H_2O,bulk}}$	$\frac{dP_{\mathrm{H_2O}}}{dx}(L) = 0$
Electric potential in Ni	$\phi_{\mathrm{el}}(0) = \eta_t$	$\frac{d\phi_{\mathrm{el}}}{dx}(L) = 0$
Electric potential in YSZ	$\frac{d\phi_{\mathrm{io}}}{dx}(0) = 0$	$\phi_{\mathrm{io}}(L) = 0$

5. Results and discussion

5.1. Microstructural parameters

From the phase-separated images, volume fractions of the three phases are calculated by counting the voxels corresponding to each phase. The obtained results are summarized in Table 3.

The ratio of the Ni volume fraction to the YSZ volume fraction is expected to be unity because the sample anode is fabricated to be Ni:YSZ = 50:50 vol.%. It is actually calculated as 1.09, 1.01 and 0.94 in each sample, respectively. This variation implies that a larger sample volume is preferred to ensure the reliability of the geometric parameters so that such statistically estimated parameters can represent the overall characteristics of the anode. On the other hand, the variation in the volume fraction ratio between the YSZ and pore phases is found to be relatively small among the three samples. Combined with the following discussion, the local nonuniformity of the tested samples is mainly attributed to the Ni phase structure.

Following the definition explained in the previous section, percolation probabilities and isolated probabilities are obtained and the results are summarized in Table 4. In the tested samples, the YSZ and pore phases have good connectivity, whereas, the connectivity of the Ni phase is very poor: and in particular, there is no percolating region in the X direction in Samples 1 and 3. On the basis of the percolation theory, a percolation probability steeply declines at a certain percolation threshold. The value of the threshold depends on the conditions such as particle size. For binary mixture of uniform-size particles, it is about 0.3 [7]. As shown in Table 3, the volume fractions of Ni and YSZ take similar values. Nevertheless the percolation probabilities of these two phases show very different trend in Table 4: the Ni phase shows a poor connectivity while the YSZ phase is connected well. It suggests difference in the microstructure that will be discussed later using the surface-to-volume ratio as an index.

The directional mean square displacements in the Ni phase of Sample 2 are shown in Fig. 6 as a typical result of the random walk calculation. In the calculation, the number of random walkers is 10^5 and the total time step is 10^7. Theoretically, the directional mean

Table 3
Volume fractions of each phase [%].

	Sample 1	Sample 2	Sample 3
Ni	27.4	25.3	24.5
YSZ	25.1	25.1	26.0
Pore	47.5	49.6	49.5

Table 4
Percolation probabilities and isolated probabilities of each phase.

		Sample 1			Sample 2			Sample 3		
		Ni	YSZ	Pore	Ni	YSZ	Pore	Ni	YSZ	Pore
Connected	X	0.000	0.966	1.000	0.477	0.943	1.000	0.000	0.958	1.000
	Y	0.582	0.966	1.000	0.477	0.943	1.000	0.411	0.958	1.000
	Z	0.867	0.966	1.000	0.842	0.943	1.000	0.724	0.958	1.000
Isolated		0.047	0.010	0.000	0.038	0.023	0.000	0.077	0.014	0.000

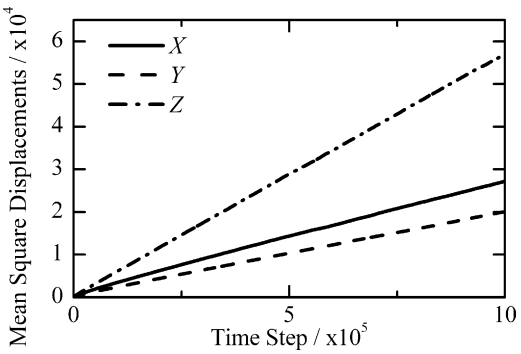

Fig. 6. Mean square displacements of random walkers in the Ni phase of Sample 2.

square displacements in the free space are $\langle x^2\rangle = \langle y^2\rangle = \langle z^2\rangle = t/3$. However, those in the porous media are smaller than those in the free space because the movement of the particles is interrupted by the obstruction effect of the phase boundaries. Following Eq. (6), we evaluated the anisotropic tortuosity factors of each phase, which is shown in Table 5. In the process of calculating the time derivatives of the mean square displacements, we omit the first 5×10^6 steps (half of the total time step) to avoid the effect of initial position of the particles. In Samples 1 and 3, it is impossible to calculate the anisotropic tortuosity factor of the Ni phase in the *X* direction because there is no percolating region in the direction. The tortuosity factors of the pore phase are relatively smaller than those in the other phases, and are similar to the values found in another report [29]. On the other hand, the Ni phase and YSZ phase have very large tortuosity factors and also a very strong anisotropic aspect. Table 5 shows that the value of tortuosity factor in *Z* direction is relatively small. If we consider that the cross-sectional area is the largest in *Z* direction, it is a sign of too small sample volume and a larger sample volume is desired. The Ni phase is obviously affected by the poor percolation probability as well, which is reasonable from Eq. (6).

The surface-to-volume ratios of each phase are summarized in Table 6. By comparison, the surface-to-volume ratio of the Ni phase is half of that of the YSZ phase. This indicates that the characteristic scale of the Ni phase is larger than that of the YSZ phase. If we assume that the volume fraction of a phase is relatively small and fixed, a small surface-to-volume ratio indicates a situation where relatively large particles are sparsely distributed in the field, which results in a limited connectivity. This is the case with the Ni phase, causing the poor connectivity and large tortuosity factors. The YSZ phase has a larger surface-to-volume ratio than the Ni phase, but their volume fractions are similar. Considering the good connectivity of the YSZ phase, the YSZ phase is expected to have a smaller structure and is more uniformly distributed. This geometric characteristic of the YSZ phase causes the complexity of the microstructural configuration and limits the transport through the phase, resulting in the large tortuosity factors. The above discussion shows that, for a given volume fraction, both very large and very small surface-to-volume ratios result in large tortuosity factors. There seems to be an appropriate range of surface-to-volume ratios for achieving effective transport in the porous structure. Note that this appropriate range of surface-to-volume ratios depends on the volume fraction.

Table 5
Anisotropic tortuosity factors of each phase.

		Sample 1			Sample 2			Sample 3		
		Ni	YSZ	Pore	Ni	YSZ	Pore	Ni	YSZ	Pore
Tortuosity factor	*X*	–	9.89	1.94	25.2	24.0	1.95	–	9.57	2.09
	Y	64.4	7.65	2.08	34.8	13.4	1.97	31.6	7.97	2.00
	Z	6.47	5.90	1.70	6.91	8.85	1.74	11.0	6.58	1.95

Table 6
Surface-to-volume ratio of each phase.

		Sample 1	Sample 2	Sample 3
S/*V* ratio [$\mu m^2\,\mu m^{-3}$]	Ni	4.51	3.56	3.83
	YSZ	8.48	7.51	7.79
	Pore	4.61	4.12	4.25

Table 7
TPB density of each sample.

	Sample 1	Sample 2	Sample 3
TPB density [$\mu m\,\mu m^{-3}$]	2.37	2.49	2.44

The characteristic length of the porous microstructure is often evaluated by particle diameter or granulometry. However it is obviously difficult to distinguish the particles one by one in the complex network structure after sintering. Therefore, we employ the surface-to-volume ratio as an index to evaluate the characteristic scale of the porous microstructure. The larger value of the surface-to-volume ratio indicates the finer structure for a given volume fraction.

The density of the TPB of each sample is summarized in Table 7. These values are slightly smaller than those reported elsewhere [29]. However, we must keep it in mind that the value strongly depends on the sample preparation.

Since the quantified parameters are applied to the numerical simulation explained in the following section, it is necessary to confirm the validity of the quantification methods to discuss errors in the numerical prediction of power generation performance. In our previous report [11], we have already confirmed the accuracy of the quantification methods for tortuosity factor and TPB density with a well-defined structure. For the tortuosity factor, the random walk simulation provides reasonable results for structure whose characteristic length is greater than 20 voxels. In this study, 20 voxels corresponds to about 1.0 μm, which is close to the particle size of the porous components, therefore, the requirement for the resolution is reasonably satisfied in the samples. The quantification error is expected to be at most 5%. For the TPB density, the requirement is less strict; the characteristic scale of the structure should be greater than 10 voxels. Therefore, the quantification error for TPB density is also expected to be less than 5%. From these evidences, we believe the methods employed in this study can provide reasonable values for the microstructural parameters.

5.2. Power generation performance

With electricity generation in electrochemical cells, we should pay attention to three voltage losses, namely, ohmic loss, activation overpotential and concentration overpotential. Assuming that the ohmic loss in the anode layer is negligibly small, the anode overpotential measured in the experiment and that set in the numerical simulation as the boundary condition are both interpreted as the sum of the activation overpotential and concentration overpotential. In this study, we define this overpotential as the "anode overpotential" and compare it between the numerical simulation and experimental results.

As presented in Section 4, various parameters related to the microstructure are needed in order to solve the governing equations (7), (8) and (10). We extracted these parameters from Sample 2 because other samples showed poor Ni phase connection as shown in Table 4. Applied values of the microstructural parameters and other computational conditions are summarized in Table 8. These values are basically kept constant in the following calculations unless specified.

Table 8
Default calculation parameters.

Parameter	Symbol	Value	Unit
Total pressure	$P_{t,\mathrm{bulk}}$	1.013×10^5	[Pa]
Temperature	T	1273	[K]
H_2 partial pressure	$P_{\mathrm{H_2,bulk}}$	$0.97 \times P_{t,\mathrm{bulk}}$	[Pa]
H_2O partial pressure	$P_{\mathrm{H_2O,bulk}}$	$0.03 \times P_{t,\mathrm{bulk}}$	[Pa]
Ni volume fraction	V_{Ni}	0.253	
YSZ volume fraction	V_{YSZ}	0.251	
Pore volume fraction	V_{pore}	0.496	
Ni tortuosity factor	τ_{Ni}	6.91	
YSZ tortuosity factor	τ_{YSZ}	8.85	
Pore tortuosity factor	τ_{pore}	1.74	
Pore S–V ratio	$(S/V)_{\mathrm{pore}}$	4.12×10^6	[$m^2\,m^{-3}$]
TPB density	l_{tpb}	2.49×10^{12}	[$m\,m^{-3}$]
Anode thickness	L	5.0×10^{-5}	[m]

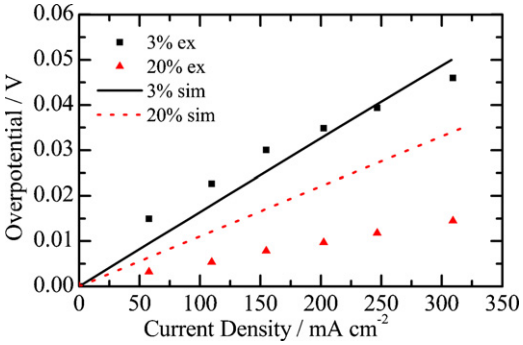

Fig. 8. Anode overpotentials in various steam concentration at 1273 K.

Fig. 7 shows typical distributions of the potentials and the volume specific current inside the anode in the thickness direction. The left end of the figure corresponds to the anode surface while the right end (50 μm) to the anode–electrolyte interface. The calculation was conducted keeping the total anode overpotential to be 0.05 V, and the average current density is calculated as 303.6 mA cm^{-2}. The volume specific current, i_{tpb}, shows the rate of the electrochemical reaction. It can be observed in this figure that the value of i_{tpb} is the largest at the anode–electrolyte interface and sharply decreases toward the anode surface direction. It shows that most of the electrochemical reaction occurs in the vicinity of the anode–electrolyte interface within about 10 μm. The thickness of the active reaction region in cermet anodes is still an open question but 10 μm seems to be reasonable for an anode having the microstructure in this study. Brown et al. [30] experimentally analyzed the reaction thickness in Ni–YSZ anode with particle diameter 0.5–1 μm, which is close to that in this study, and reported the reaction thickness is about 10 μm. Shikazono et al. [14] conducted 3D numerical simulation using the same anode structure as we use in this study, and reported the similar reaction thickness around 10–15 μm. Since the hydrogen supply is enough for the reaction rate in this case, the effect of concentration overpotential is small. Note that the concentration overpotential is graphically expressed as the gap between the black line and the blue line. The activation overpotential, which is expressed as the gap between the blue and the red lines, naturally becomes large near the anode–electrolyte interface where the electrochemical reaction is prominent. The figure shows that the activation overpotential is the major cause of the voltage loss and it occurs in the vicinity of the anode–electrolyte interface.

Calculations are conducted varying the anode overpotential and the gas compositions (x% $H_2O-(100-x)$% H_2, x = 3, 10, 20) of the fuel. Except for the gas compositions, calculation parameters shown in Table 8 are used. Fig. 8 compares the anode overpotential predicted by the simulation and its experimental counterpart. The predicted overpotential agrees fairly well with the experimental counterpart at 3% humidified condition. When the steam concentration is raised to 20%, the anode overpotential decreases in the experiment and the simulation qualitatively captures this phenomenon. However the anode overpotentials are about twice overestimated in the high humidified condition. This may be because of the empirical relationship used for the exchange current density per unit volume $i_{0,\mathrm{tpb}}$ (Eq. (26)). In the relationship, it is possible that the catalytic activity of steam is underestimated. Another possible reason of the discrepancy is the effect of the local high steam concentration around TPBs. In the polarized condition, electrochemical reaction produces steam, which causes high steam concentration locally around the TPBs. Such a local high steam concentration can decrease the activation overpotential. A similar discrepancy between the simulation and experiment for high steam condition is, however, reported by Shikazono et al. [14] who applied Lattice Boltzmann Method (LBM) and carried out calculation based on actual 3D porous structure obtained from FIB–SEM. Further investigation is needed to understand the phenomenon under a high steam concentration.

Fig. 9 shows the effect of the operating temperature on the anode overpotential. Except for the temperature, calculation parameters shown in Table 8 are used. The predicted overpotential agrees fairly well with the experimental counterpart at 1273 K. The anode overpotential increases as the operating temperature is decreased in the experiment. The 1D simulation can reproduce this tendency but in the low temperature conditions, 1173 and 1073 K, it is overestimated especially in the large current density region. The local high steam concentration mentioned previously may also be the reason of the overestimation. Another possible reason is the effect of the activation energy used in the exchange current density model (Eq. (26)). Bieberle et al. [31] reported smaller activation energy

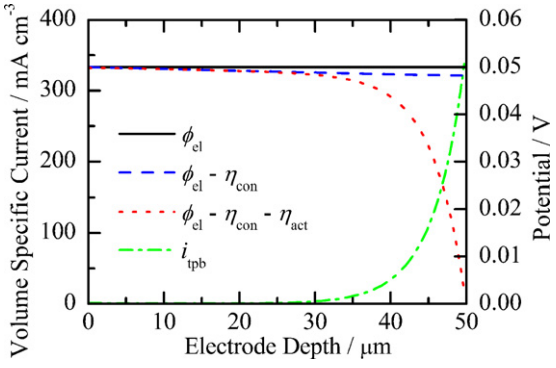

Fig. 7. Volume specific current and potential distributions in the default case. Total anode overpotential is set to be 0.05 [V]. Average current density is 303.6 mA cm^{-2}.

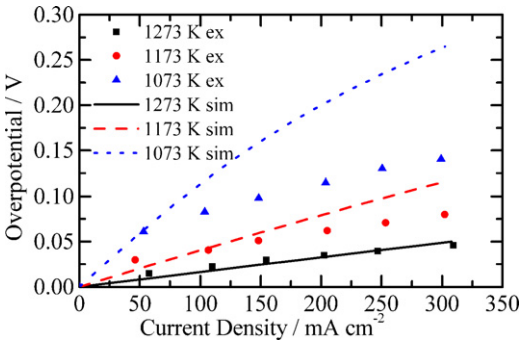

Fig. 9. Anode overpotentials in various temperatures at 3% humidified condition.

in the H_2 oxidation on the Ni pattern electrode. Smaller activation energy may be able to represent the temperature dependence more close to the experimental results; however, the value of the exchange current density estimated from his experiment is two orders higher than that reported by de Boer [27]. Therefore, it is still difficult to obtain reasonable values of overpotentials in low temperature condition.

In the previous section, we discussed the quantification error in the microstructural parameters. The expected error is at most 5% for both tortuosity factor and TPB density. In our previous report [32], we conducted sensitivity analysis to investigate the effects of variation in the microstructural parameters on the power generation performance. From the analysis, the largest error in the current density is expected to be less than 3%, which poses no significant problem on the discussion in this paper.

6. Conclusions

The three-dimensional microstructure of a porous anode of an SOFC is directly observed by a focused ion beam and scanning electron microscope (FIB–SEM). Microstructural parameters which are related to transport phenomena in porous media are quantitatively evaluated, such as volume fraction, percolation probability, tortuosity factor, surface-to-volume ratio, and three-phase boundary density.

For achieving high performance anode, higher transport characteristics and more reaction sites are required: low tortuosity factor and large TPB density. In the tested samples, both the Ni and YSZ phases have large tortuosity factors, which are unfavorable for electron and ion transport through the phases. In order to optimize the microstructure, we need to properly adjust surface-to-volume ratio and volume fractions to reduce the structural complexity. For instance, larger surface-to-volume ratio for Ni phase is effective to ensure sufficient connectivity. In contrast, smaller surface-to-volume ratio for YSZ phase is effective to reduce the complexity of the microstructural configuration. However, low structural complexity may result in decreasing reaction site. Therefore, further investigation about the relationships among microstructural parameters is required.

A 1D numerical simulation to predict the anode polarization characteristics is conducted without using any micro model but directly applying the microstructural parameters evaluated from the reconstructed 3D structure. The predicted overpotential agrees well with the experimental counterparts in the condition of the low steam concentration (3%) and high temperature (1273 K). The effects of steam concentration and temperature are qualitatively reproduced, but the values are overestimated in high steam concentration (20%) and low temperature (1173, 1073 K) conditions.

The small sample volume is considered to be the reason of high anisotropic aspects in the quantified microstructural parameters and large discrepancy between the numerical simulation and experimental results. More systematic analysis with larger sample volume will be reported in the future.

Acknowledgements

This work is supported by the New Energy and Industrial Technology Development Organization (NEDO) under the Development of System and Elemental Technology on Solid Oxide Fuel Cell (SOFC) Project.

References

[1] D. Simwonis, F. Tietz, D. Stöver, Solid State Ionics 132 (2000) 241–325.
[2] J.-H. Lee, H. Moon, H.-W. Lee, J. Kim, J.-D. Kim, K.-H. Yoon, Solid State Ionics 148 (2002) 15–26.
[3] D.S. McLachlan, Solid State Physics 20 (1987) 865–877.
[4] J. Gurland, Transactions of the Metallurgical Society of AIME 212 (1958) 452–455.
[5] Z. Fan, A.P. Miodownik, P. Tsakiropoulos, Material Science and Technology 9 (1993) 1094–1100.
[6] S. Sunde, Journal of The Electrochemical Society 142 (1995) L50–L52.
[7] P. Costamagna, P. Costa, V. Antonucci, Electrochimica Acta 51 (2006) 3446–3460.
[8] J.R. Wilson, W. Kobsiriphat, R. Mendoza, H.-Y. Chen, J.M. Hiller, D.J. Miller, K. Thornton, P.W. Voorhees, S.B. Adler, S.A. Barnett, Nature Materials 5 (2006) 541–544.
[9] K. Thyden, Ph.D. thesis, Technical University of Denmark, 2008.
[10] J.R. Smith, A. Chen, D. Gostovic, D. Hickey, D. Kundinger, K.L. Duncan, R.T. DeHoff, K.S. Jones, E.D. Wachsman, Solid State Ionics 180 (2009) 90–98.
[11] H. Iwai, N. Shikazono, T. Matsui, H. Teshima, M. Kishimoto, R. Kishida, D. Hayashi, K. Matsuzaki, D. Kanno, M. Saito, H. Muroyama, K. Eguchi, N. Kasagi, H. Yoshida, Journal of Power Sources 195 (2010) 955–961.
[12] P.R. Shearing, J. Gelb, N.P. Brandon, Journal of the European Ceramic Society 30 (2010) 1809–1814.
[13] T. Matsui, R. Kishida, J.-Y. Kim, H. Muroyama, K. Eguchi, Journal of the Electrochemical Society 157 (5) (2010) B776–B781.
[14] N. Shikazono, D. Kanno, K. Matsuzaki, H. Teshima, S. Sumino, N. Kasagi, Journal of The Electrochemical Society 157 (5) (2010) B665–B672.
[15] J.R. Wilson, J.S. Cronin, A.T. Duong, S. Rukes, H.-Y. Chen, K. Thornton, D.R. Mumm, S. Barnett, Journal of Power Sources 195 (2010) 1829–1840.
[16] Y. Nakashima, S. Kamiya, Journal of Nuclear Science & Technology 44 (9) (2007) 1233–1247.
[17] M. Kishimoto, H. Iwai, M. Saito, H. Yoshida, ECS Transactions 25 (2) (2009) 1887–1896.
[18] J.R. Wilson, M. Gameiro, K. Mischaikow, W. Kalies, P.W. Voorhees, S.A. Barnett, Microscopy and Microanalysis 15 (2009) 71–77.
[19] U. Anselmi-Tamburini, G. Chiodelli, M. Arimondi, F. Maglia, G. Spinolo, Z.A. Munir, Solid State Ionics 110 (1998) 35–43.
[20] N.F. Bessette II, W.J. Wepfer, J. Winnick, Journal of The Electrochemical Society 142 (11) (1995) 3792–3800.
[21] E.A. Mason, A.P. Malinauskas, R.B. Evans III, The Journal of Chemical Physics 46 (8) (1967) 3199–3216.
[22] D. Aronšt, P. Schneider, The Chemical Engineering Journal 57 (1995) 91–99.
[23] E.N. Fuller, P.D. Schettler, J.C. Giddings, Industrial Engineering Chemistry Research 58 (5) (1966) 19–27.
[24] R.H. Perry, Perry's Chemical Engineers' Handbook, 7th ed., McGraw-Hill, New York, 1981.
[25] M. Kaviany, Principles of Heat Transfer in Porous Media, Springer-Verlag, 1991.
[26] A. Konno, H. Iwai, M. Saito, H. Yoshida, Thermal Science and Engineering in Japanese 18 (3) (2010) 103–114.
[27] B. De Boer, Ph.D. thesis, University of Twente, The Netherland, 1998.
[28] Y. Suzue, N. Shikazono, N. Kasagi, Journal of Power Sources 184 (2008) 52–59.
[29] J.R. Wilson, S.A. Barnett, Electrochemical and Solid-State Letters 11 (10) (2008) B181–B185.
[30] M. Brown, S. Primdahl, M. Mogensen, Journal of The Electrochemical Society 147 (2) (2000) 475–485.
[31] A. Bieberle, L.P. Meier, L.J. Gauckler, Journal of The Electrochemical Society 148 (6) (2001) A646–A656.
[32] M. Kishimoto, H. Iwai, M. Saito, H. Yoshida, Proceedings of the 14th International Heat Transfer Conference, IHTC-22495, 2010.